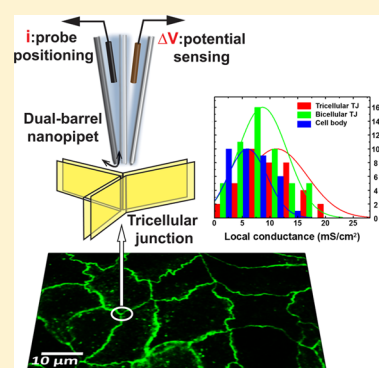


Capturing Rare Conductance in Epithelia with Potentiometric-Scanning Ion Conductance Microscopy

Lushan Zhou,[†] Yongfeng Gong,[‡] Abby Sunq,[‡] Jianghui Hou,^{*,‡,§} and Lane A. Baker^{*,†}[†]Department of Chemistry, Indiana University, 800 E. Kirkwood Avenue, Bloomington, Indiana 47405, United States[‡]Renal Division, Washington University Medical School, 660 South Euclid Avenue, St. Louis, Missouri 63110, United States[§]Center for Investigation of Membrane Excitability Diseases, Washington University Medical School, 660 South Euclid Avenue, St. Louis, Missouri 63110, United States

Supporting Information

ABSTRACT: Tight junctions (TJs) are barrier forming structures of epithelia and can be described as tightly sealed intercellular spaces. Transport properties have been extensively studied for bicellular TJs (bTJs). Knowledge of the barrier functions of tricellular junctions (tTJs) are less well understood, due largely to a lack of proper techniques to locally measure discrete tTJ properties within a much larger area of epithelium. In this study, we use a nanoscale pipet to precisely locate tTJs within epithelia and measure the apparent local conductance of tTJs with a technique termed potentiometric scanning ion conductance microscopy (P-SICM). P-SICM shows the ability to differentiate transport through tTJs and bTJs, which was not possible with previous techniques and assays. We describe P-SICM investigations of both wild type and tricellulin overexpression Madin-Darby Canine Kidney (strain II, MDCKII) cells.



Epithelia are known as important barriers for regulation of the transport of ions, water, and large solutes. Sealing of intercellular spaces within epithelial layers is critical to establish barrier functions and is achieved by formation of tight junctions (TJs) which regulate paracellular transport.^{1–5} Interestingly, heterogeneity present in paracellular transport pathways remains largely unexplored, and barrier transport properties are typically described in the context of the majority junction, bicellular tight junctions (bTJs), formed at the interface of two adjacent cells. However, at intercellular contact points where three or more cells meet, unique cellular junctions are formed, referred to as tricellular tight junctions (tTJs).⁶ Ultrastructurally, tTJs differ drastically from bTJs. bTJs are composed of a series of direct intercellular membrane contacts¹ and form bTJ channels that are nominally 4–7 Å in diameter^{7,8} and a few nanometers long.⁹ tTJs are formed from at least three pairs of vertically extended TJ strands and appear as “central tubes” that are ~1 μm in length and ~10 nm in diameter, as observed from freeze-fracture replica electron microscopy.¹⁰ The significant differences of bTJs and tTJs, both in structure and in protein composition, result in marked differences in transport properties.^{6,11,12} However, differentiation of bTJ and tTJ transport remains challenging due to the lack of recording approaches that can capture the relatively rare tTJ specific conductance. With a combination of fluorescence microscopy, electrical measurements, and a geometric model, Krug et al. estimated the contribution of tTJ conductance relative to the overall paracellular conductance.¹² Considering the highest value possible for the conductance of a single tTJ, the total tTJ contribution was estimated to be only ~1% of the total

paracellular conductance. This estimation underscores the fact that even though channels formed at tTJs are physically larger than bTJs, the much smaller population of tTJs relative to bTJs results in a smaller net contribution from tTJs.^{12–14} For tighter (more resistive) epithelia such as the blood-brain barrier, the consequences of tTJ conductance may be of greater significance. Taken in total, the smaller overall population and related low density of tTJs results in conductance from tTJs being considered as “rare”¹² in terms of the total paracellular conductance.

To record transport at tTJ channels and to study tTJ transport properties, a method with both high spatial resolution and high sensitivity is needed. Previous methods to record epithelial transport, such as transepithelial electrical resistance (TER)¹⁵ and impedance spectroscopy,^{16,17} record the response from the entire exposed area of a cell monolayer (typically thousands of cells). The further development of two-path impedance spectroscopy provided a way to separate contributions from paracellular versus transcellular pathways within an epithelial cell layer.¹⁸ However, heterogeneity in paracellular transport still could not be identified. Local measurement approaches include microelectrode voltage/conductance scanning described by Fromm and co-workers.^{9,12,19–21} Although successful in differentiation of conductance at individual bicellular contacts and over single cells in an epithelium,

Received: June 21, 2016

Accepted: September 12, 2016

Published: September 12, 2016

instrumental limitations in previous voltage scanning approaches, combined with the rare nature of tTJ conductance, prevented measurement of tTJs directly. However, geometric considerations of physical dimensions predict an obvious difference in ionic conductance between an individual tTJ central tube (146 pS in Ringer's solution¹²) and an individual bTJ channel (e.g., 70–100 pS in Ringer's solution for claudin-2 pore⁹).

Herein, we report the use of potentiometric scanning ion conductance microscopy (P-SICM),²² an advanced form of previous voltage scanning instruments, to provide nanoscale electrode positioning. P-SICM is a modified version of scanning ion conductance microscopy (SICM),²³ a noncontact scanning probe technique suitable for live-cell imaging in physiological buffer. The use of a dual-barrel nanopipet (Figure 1) as both an

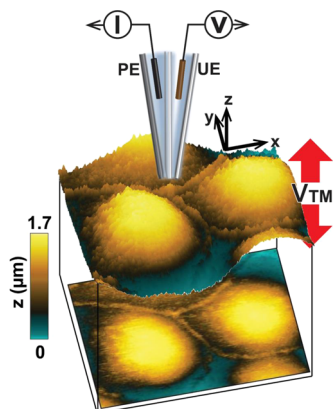


Figure 1. Schematic of potentiometric scanning ion conductance microscopy (P-SICM) measurement at a tricellular tight junction (tTJ). The pipet electrode (PE) in one barrel of the dual-barrel probe records topography and controls pipet position. Potential gradients over different features are induced by an applied transepithelial voltage (V_{TM}) across the cell monolayer and are captured with the potentiometric electrode (UE) in the second barrel. V_{TM} is applied through three bulk electrodes (not shown here, see Figure S1a).

imaging and measuring probe in P-SICM achieves precise probe control/sensing at nanometer scales. As demonstrated previously, potentiometric measurement in P-SICM provides enhanced signal-to-noise ratios (relative to normal ion current recording^{22,24,25}), a critical parameter for differentiating tTJ transport from overall epithelial transport. With precise positioning and high sensitivity, P-SICM effectively defines a confined nanoscale sensing zone at the pipet tip which can spatially differentiate tTJ and bTJ conductance.

To quantify paracellular conductance heterogeneity (tTJ vs bTJ) in epithelia, we chose to examine conductance changes related to the protein tricellulin, the first and one of the most important integral membrane proteins found in tTJ “central tubes”.⁶ Tricellulin is concentrated at tTJs and has been shown necessary for maintenance of tTJ structure integrity and barrier functions.^{6,26–29} In addition to the role of tricellulin in tTJs, previous electron microscopy studies have found that tricellulin overexpression in bTJs also leads to more continuous bTJ strands.¹² However, detailed knowledge of tricellulin effects on tTJ vs bTJ channel permeability is scarce due to the lack of proper analytical tools. Epithelial cell monolayers from the well characterized Madin-Darby Canine Kidney strain II (MDCKII) cell line were used in this study, as wild type MDCKII cells exhibit low endogenous expression levels of tricellulin.¹² We

detail P-SICM measurements for both wild type and tricellulin overexpression MDCKII cell lines to examine the effect of tricellulin on tTJs and bTJs.

EXPERIMENTAL SECTION

Nanopipet Fabrication. Dual-barrel nanopipets were pulled from theta quartz capillaries (QT120-90-7.5, Sutter Instrument, Novato, CA) with a CO₂-laser puller (P-2000, Sutter Instrument), pulling parameters: Heat = 700, Fil = 3, Vel = 40, Del = 150, Pull = 160. Nanopipet tip sizes (coated with Au/Pd) were characterized with scanning electron microscopy (SEM, FEI Quanta-FEG, Hillsboro, OR). Figure 2a inset shows

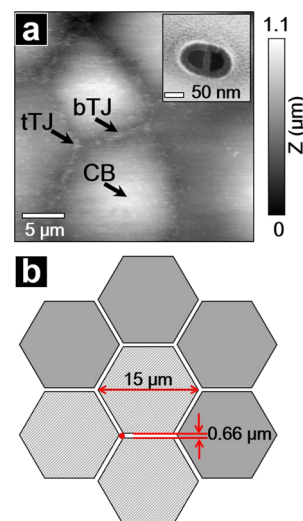


Figure 2. (a) Topographic image of the apical surface of a MDCKII cell monolayer grown on a P-SICM perfusion cell. Tricellular, bicellular tight junctions (tTJ, bTJ) and cell body (CB) can be clearly identified. Scanning electron micrograph of the end-on view of a typical dual-barrel nanopipet used in the P-SICM (inset). (b) Diagram of a uniform hexagonal network representing epithelial cell topology. The circumradius of each hexagon, which represents a single cell in a monolayer, is assigned to be 7.5 μm . The red dot at one triple contact area represents a tTJ with 0.66 μm diameter, determined from SICM (see Figure S1 for details). Area percentage in the total area of one cell monolayer for tTJ, bTJ, and CB are estimated to be 0.4%, 9.2%, and 90.4%, respectively.

a representative SEM image of the nanopipet tip. The inner diameters of each barrel were determined to be 49 and 45 nm and represent typical dimensions for pipets used in this study. Both barrels of the theta pipet were filled with phosphate-buffered saline (PBS), and Ag/AgCl electrodes were inserted into each barrel for current and potential sensing, respectively.

P-SICM Instrumentation. A ScanIC scanning ion conductance microscope (Ionscope, London, UK), modified for P-SICM and incorporating an Axopatch 200B current amplifier (10 k Ω input impedance), was used to measure the apparent local conductance at cell monolayers (vide infra) as described previously.²² (We underscore here that the values measured are apparent conductances, as opposed to absolute conductances. Apparent conductances are valid for comparisons made in this report.) A dual-barrel nanopipet is used as a scanning probe and is placed in the top chamber of the perfusion cell (apical side of the cell monolayer). One barrel of the probe, termed the pipet electrode (PE), measures the probe-surface distance (D_{ps})-dependent ion current and controls the positioning of the

probe. The second barrel, termed the potentiometric electrode (UE) senses the local electric field with respect to a bulk reference electrode (RE) in the bath solution. A transepithelial potential (V_{TM}) is applied across the cell monolayer via three bulk electrodes (not shown in the schematic in Figure 1), the RE and counter electrode (CE) in the top chamber and a working electrode (WE) in the bottom chamber (Figure S1a). To avoid depolarization and disruption of physiological functions of the cell monolayer, a small amplitude alternating transepithelial potential was utilized (typically a triangle wave at 1 Hz, ± 50 mV).

To measure the apparent local conductance (G) at any point above the cell monolayer, the probe was positioned at the point of interest, and local potential deflections (ΔV) were recorded at the UE for two different D_{ps} (0.2 and 12.5 μm). The value of G can then be approximated from eq 1.^{19,30}

$$G = \left(\frac{(\Delta V_{0.2\mu\text{m}} - \Delta V_{12.5\mu\text{m}}) / \Delta z}{\rho V_{\text{TM}}} \right) \quad (1)$$

In eq 1, the ratio of the difference in local potential deflections ($\Delta V_{0.2\mu\text{m}} - \Delta V_{12.5\mu\text{m}}$) and the probe displacement (Δz) estimates the local electric field, which is further divided by bath electrolyte resistivity (ρ) and V_{TM} to give the apparent local conductance. Potentiometric measurements were used due to benefits in signal intensity and signal-to-noise ratio, relative to ion current measurements with high impedance nanopipets.^{22,24} Results from measurements were subjected to statistical tests as described in the Supporting Information. Significance levels are denoted as * $p < 0.05$, ** $p < 0.01$, *** $p < 0.001$, **** $p < 0.0001$.

Large Cation Replacement Experiment. Madin-Darby Canine Kidney strain II (MDCKII) cell lines, wild type (MDCKII-WT, from ATCC, Manassas, VA) and a tricellulin overexpression mutant (MDCKII-Tric) were seeded onto a two-chamber perfusion cell and bulk impedance analysis was performed before P-SICM measurements (see the Supporting Information for details). Local conductances at discrete points (e.g., over a tTJ, bTJ, or cell body) were measured for both cell lines first with Ringer's solution (buffer A, Supporting Information), on both apical and basolateral sides. Then, to study size selective transport at TJ, the basolateral solution was changed to buffer B (5 mM NaCl, 149 mM NMDG-Cl, 5 mM KCl, 1 mM MgCl_2 , 2 mM CaCl_2 , 8 mM mannitol, and 10 mM HEPES, pH 7.40), in which the majority of Na^+ is replaced with isomolar *N*-methyl-D-glucamine (NMDG^+), a large cation (mean diameter ~ 7.29 Å³¹) known to be impermeable to transcellular and bTJ paracellular channels.³²

RESULTS AND DISCUSSION

P-SICM for Detecting Rare Conductance in a Cell Monolayer. We have previously described P-SICM studies that combined noncontact nanoscale imaging of live cells with local electrical measurements at bTJs.^{22,25} In a topographic image of a MDCKII cell monolayer recorded with SICM (Figure 2a), tTJs, the subject of the study here, can be clearly distinguished from bTJs and the cell body (CB). Since, relative to bTJs, tTJs make up a smaller fraction of the total area of a cell monolayer, bulk electrophysiological measurements cannot easily measure the conductance at tTJs. The "rareness" of tTJ conductance can be estimated with a very simple consideration of area ratios of different transport pathways within a monolayer.

As shown in Figure 2b, we adopt a uniform hexagonal network with evenly distributed spacing between neighboring hexagons as a reduced polygonal model of a cell monolayer, an accepted approach to model epithelia.^{33,34} Each hexagon approximates an individual epithelial cell (diameter of each hexagon is 15 μm , nominally equivalent to the size of a single MDCKII cell), with tTJs and bTJs formed at relevant contact points between cells. In Figure 2b, a tricellular contact is indicated as a red circle with a diameter of 0.66 μm , as determined from the fwhm of the topographical feature located at a tTJ (Figure S1), as recorded by SICM. The effective dimension for a tricellular contact instead of tTJ central tube diameter is used here to estimate the sensing zone of SICM in measuring tTJs. For one tTJ area (formed with three cells that are hatched fill in Figure 2b) the total areas (with consideration of neighboring cells) for tTJ (A_{tTJ}), bTJ (A_{bTJ}), and CB (A_{CB}) can be calculated to as 0.342 μm^2 , 7.44 μm^2 , and 73.2 μm^2 . A_{tTJ} is only 0.4% of the total cell monolayer and 9.2% of the total paracellular areas, which makes it very challenging to capture transport at tTJ channels from ensemble measurements. Again, the 0.66 μm diameter is likely an overestimation of the actual tTJ area within the cell monolayer, but this number represents the tTJ area sensed by the SICM probe in imaging including practical factors, such as tip convolution. Therefore, 0.66 μm provides the practical "rareness" of tTJ estimation under P-SICM measurements. Electron microscopy (Figure 2a) of the dual-barrel nanopipet tip opening shows the diameter of each barrel is ~ 50 nm, which compares well with the estimated tTJ area. Experimental and simulation studies of SICM resolution have determined objects laterally spaced about two to three times of the tip inner radii (r_i) or more can be resolved by SICM. However, experimental factors including object shape, object height, and especially scan height (or D_{ps}) can affect the practical resolutions, and SICM resolution as low as $0.5r_i$ has been reported.^{35–39} For P-SICM measurements, we consider the tip as a sensing probe for measuring local electric field or potential gradient, which has a spatial distribution determined from the conductive pathways in the sample. To address resolution with P-SICM, a best case scenario based on the Newman model⁴⁰ can be used to estimate conductances measured over well-defined nanoscale pores present in an insulating substrate. In previous work⁴¹ and here (see below and the Supporting Information), we have calculated the potential profiles above nanopores (e.g., 1–500 nm diameter) at a given D_{ps} . The maximum potential response (recorded at the center of the pore) decreases by $\sim 60\%$ within 1 μm and by $\sim 90\%$ within 2 μm when the probe is translated laterally from the pore center. These simulations suggest that at least for conductive pathways spaced 2 μm apart, the field overlap is minimal and the nanopipet will sense at most 10% of the signal coming from a conductive pathway 2 μm away from the feature under measurement. For the studies here, we compare relative differences in conductance, and as such the signals measured are more complex, dynamic, and more challenging, as the substrate itself (the cell monolayer) has an intrinsic conductance contribution, as it is not a perfect insulator.

Differentiation of the Conductance of Tricellular Pathway from the Bicellular and Transcellular Pathways with P-SICM. To record the apparent local conductance (G), the pipet is positioned over discrete locations (tTJs, bTJs, and CB) within the cell monolayer according to the topographic image. The local electric field is captured by sensing potential deflections (ΔV) with the potentiometric barrel (UE) under an

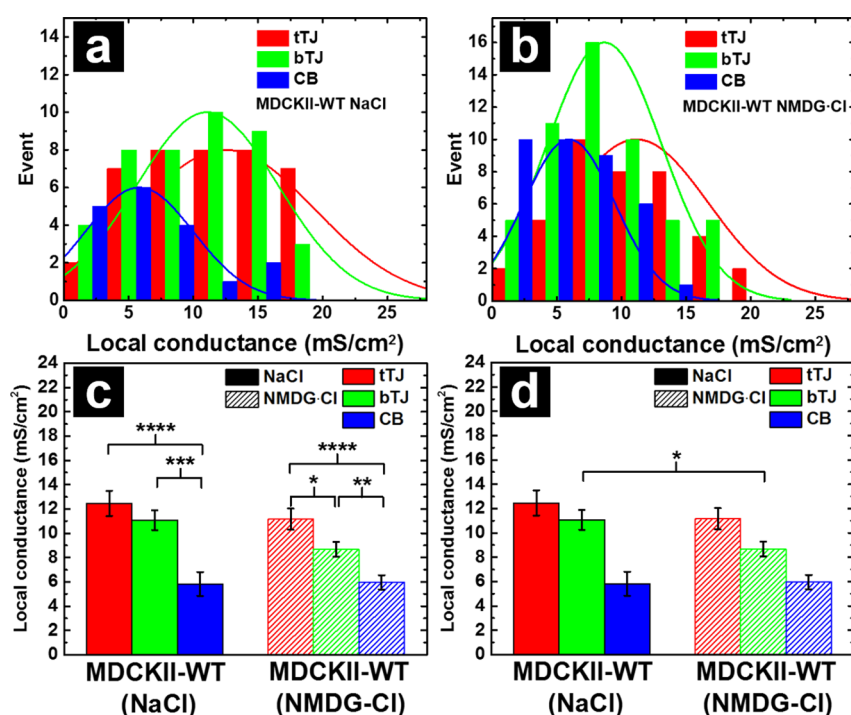


Figure 3. Histograms of P-SICM recording of local conductance values measured over tTJ, bTJ, and CB for MDCKII wild type cells in (a) Ringer's solution and in (b) NMDG⁺ replacement solution. Average values of each type of measurement in parts a and b are shown in parts c and d. (c) Statistical analysis indicates P-SICM not only can differentiate para- and transcellular transport pathways but also can differentiate paracellular transport (tTJ vs bTJ) in the NMDG⁺ replacement experiment ($p < 0.05$). (d) NMDG⁺ substitution for Na⁺ induced a significant decrease in bTJ conductance ($p < 0.05$), but not in tTJ and CB conductance, indicating this large cation cannot permeate bTJ pores and cell membranes but can transport through tTJs. All statistical test results are in the [Supporting Information](#).

Table 1. Apparent Local Conductance Values^a

G (mS/cm ²)	WT (NaCl)	WT (NMDG-Cl)	Tric overexpress (NaCl)	Tric overexpress (NMDG-Cl)
tTJ	12.47 ± 1.04 ($n = 44$) ^b	11.16 ± 0.87 ($n = 41$)	10.44 ± 0.67 ($n = 44$)	10.49 ± 0.60 ($n = 89$)
bTJ	11.08 ± 0.82 ($n = 45$)	8.67 ± 0.61 ($n = 52$)	8.35 ± 0.63 ($n = 41$)	6.86 ± 0.49 ($n = 72$)
CB	5.83 ± 0.99 ($n = 18$)	5.95 ± 0.59 ($n = 36$)	5.34 ± 0.62 ($n = 28$)	5.32 ± 0.57 ($n = 29$)

^aValues presented as mean ± SEM. ^b n , sample size.

applied transepithelial voltage at a close distance ($D_{ps} \sim 200$ nm) and a far distance ($D_{ps} \sim 12.5$ μ m). As shown in [eq 1](#), the local electric field (E) is determined as the average gradient of local potential and is then used to obtain G values.

P-SICM measurements of MDCKII-WT samples in NaCl based Ringer's solution are shown in histograms in [Figure 3a](#) and in [Table 1](#). More than three monolayers were tested for experiments in each recording buffer. The apparent local conductance for tTJ, bTJ, and CB obey a normal distribution as examined with the Shapiro-Wilk test (Table S1, [Supporting Information](#)). The average G values are 12.47 ± 1.04 mS/cm² ($n = 44$) for tTJ, 11.08 ± 0.82 mS/cm² ($n = 45$) for bTJ, and 5.83 ± 0.99 mS/cm² ($n = 18$) for CB. Both types of paracellular transport pathways (G^{tTJ} , G^{bTJ}) are more conductive than the transcellular pathway (G^{CB}) with higher G values that are statistically different from G^{CB} (independent two-sample t test $p < 0.0001$ for G^{tTJ} vs G^{CB} , $p < 0.001$ for G^{bTJ} vs G^{CB} ; Table S2, [Supporting Information](#)). The p -value of 0.3 between G^{tTJ} and G^{bTJ} indicates no statistical difference in the conductance of tTJ and bTJ channels. One possible reason is that since tTJs are isolated as discrete channels in the cell monolayer, only one tTJ channel is underneath the probe. Considering a tTJ channel is only 10 nm in diameter while the P-SICM effective sensing area is nominally submicrometer, contributions from conductance of

multiple bTJ channels in flanking bTJs may contaminate the signal from tTJ during measurement. Thus, the "bTJ background" in tTJ conductance recording likely averages out the characteristic response from tTJ and hence differences between the measured G values of the two TJJs. Similar effects due to surrounding transcellular transport pathways have been discussed in a previous theory paper⁴¹ (details related to the local potential distribution and overlap are discussed further vide infra).

To differentiate tTJ and bTJ transport, ion replacement experiments were carried out with the same MDCKII-WT cells. In the ion replacement experiment, Na⁺ in the basolateral bath solution was substituted with isomolar NMDG⁺, an organic cation that is too large (7.29 Å mean diameter³¹) to permeate bTJs but is small enough to permeate tTJs with minimal hindrance. P-SICM results are shown as histograms ([Figure 3b](#), values listed in [Table 1](#)) and as bar graphs ([Figure 3c,d](#), right panel). With size dependent ion permeation, tTJs and bTJs were clearly differentiated as two unique ($p < 0.05$), normally distributed populations (Tables S1 and S2, [Supporting Information](#)). This result confirms that tTJ and bTJ are two different types of paracellular channels with different sizes and transport properties, and P-SICM provides a powerful tool to

capture such heterogeneous events with submicrometer resolution.

Comparison of recordings in Ringer's solution and in NMDG⁺ substitution buffer revealed a significant decrease in G^{bTJ} to 8.67 ± 0.61 mS/cm² (22%, $p < 0.05$, Figure 3d). G^{tTJ} also decreased to 11.16 ± 0.87 mS/cm² (10%), but a statistical test indicated the change was not significant. From a measurement point of view, the decrease in G^{tTJ} could be due to the "bTJ background" in P-SICM recording as mentioned above. Thus, the large decrease in G of the adjacent bTJs may have induced the corresponding change in tTJ. From an ion transport point of view, one NMDG⁺ ion carries the same charge as one Na⁺ ion; however, NMDG⁺ can experience more steric hindrance when traversing tight junctions. Overall, these data demonstrate that P-SICM provides a valuable tool both to sense rare tTJ conductance in biological specimens and to distinguish the conductance of different types of paracellular transport pathways within live cell monolayers for the first time.

P-SICM Studies the Role of Tricellulin in TJ Transport.

Transport properties at bTJs have been probed by extensive studies of claudin proteins,^{31,42–45} while comparable knowledge at tTJs is lacking. Above, we have shown with P-SICM measurements that tTJs differ from bTJs in transepithelial transport. We now further explore the function of tricellulin, the first known tTJ protein, in TJ transport and the effect of tricellulin on both types of TJ channels. MDCKII cells overexpressing tricellulin (MDCKII-Tric) with concomitant expression of green fluorescent protein (GFP) marker were generated with the previously described retroviral protocol utilizing the internal ribosome entry site (IRES).²⁵ Figure 4a shows a fluorescence microscopy image of an MDCKII-Tric cell monolayer. Green cells which express GFP have a concomitant increase in expression level of tricellulin compared to wild type cells. Fluorescence activated cytometry sorting (FACS) was performed on MDCKII-Tric cells prior to seeding to ensure ~80–90% or more cells overexpress tricellulin with GFP marker (see the Supporting Information). Western blot analyses of FACS sorted green cells showed a 10.19-fold increase in tricellulin protein expression levels (Figure S3A,B), compared to MDCKII-WT cells. Confocal microscopic imaging of the MDCKII-Tric cell monolayers revealed that subcellular tricellulin protein localization was not only reinforced in the tTJs but also extended to the bTJs (Figure S4).

Bulk impedance spectra of both MDCKII-WT and MDCKII-Tric monolayers grown on P-SICM perfusion cell filters were examined and shown in Figure 4b. Transepithelial electrical resistance (TER) was found to increase with higher tricellulin expression levels, indicating the function of tricellulin in tightening the epithelial barrier. However, as discussed in the introduction, impedance measurements report a response from all transport pathways in a cell monolayer and the observed difference between MDCKII-WT and -Tric cells cannot be attributed to specific changes in tTJs, bTJs, or CB. In other words, bulk impedance spectroscopy lacks information and quantitation of how individual components of G^{tTJ} , G^{bTJ} , and G^{CB} are altered in MDCKII-Tric cells in the total TER, let alone changes for individual cell–cell junctions. P-SICM, combined with fluorescence microscopy, allows investigation of individual tTJs and bTJs formed between tricellulin overexpression cells to be located and measured.

P-SICM recordings of MDCKII-Tric cells in Ringer's solution were compared to MDCKII-WT cells first (Figure 5a). Paracellular conductance decreased in the tricellulin

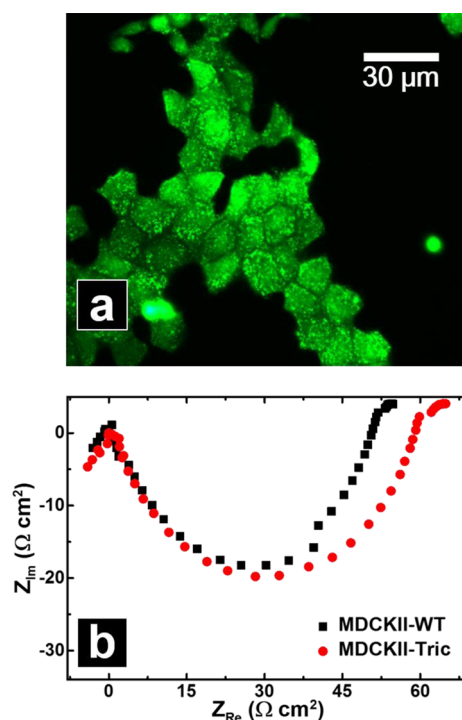


Figure 4. (a) Fluorescence image of tricellulin overexpression MDCKII (MDCKII-Tric) cells. Cells with GFP marker express higher levels of tricellulin than the dark cells, which have low endogenous tricellulin expression. (b) Representative Nyquist plot of impedance spectra recorded from MDCKII-WT (black square) and MDCKII-Tric (red circle) cell monolayers grown on P-SICM perfusion cell filters (fluorescence images of representative samples are shown in Figure S2c,d, Supporting Information). (*Values are corrected to make the semicircles corresponding to cell monolayer response start from 0 Ω cm², with values before zero representing impedance responses from the supporting PET filter membrane.)

overexpression sample, while transcellular conductance was not altered. This result indicates that tricellulin, similar to other TJ proteins such as claudins, primarily regulates transport across intercellular spaces. A ~16% ($p = 0.1$) decrease in G^{tTJ} was observed and is less significant than the ~25% reduction of G^{bTJ} ($p < 0.01$). The change in G^{bTJ} induced by tricellulin overexpression is likely due to the 50% reduction in claudin-2 protein expression (Figure S3C). Claudin-2 bTJ localization appeared to be unchanged (Figure S4). In a previous study of ultrastructural changes in bTJ networks in tricellulin overexpression MDCKII cells,¹² overexpressed tricellulin was shown to extend and locate at bTJs, causing a reduction in breaks or discontinuities of bTJ strands. Such changes in the ultrastructure may also result in a decrease in bTJ permeability and hence G^{bTJ} , while the small and insignificant reduction in G^{tTJ} may result from the altered "bTJ background" during P-SICM recording over tTJ areas, as described vide supra. The tTJ "central tube" itself should, however, not change in dimension with the overexpression of tTJ proteins. A previous freeze-fracture electron microscopy study also showed that overexpressed tricellulin increases tTJ horizontal strands that extend to bTJs but did not appear to affect tTJ diameter.¹² In other words the basic transport properties of tTJs should not change, especially for ions (e.g., Na⁺) that are much smaller than the tTJ "central tubes". On the basis of this, we attribute the slight decrease in G^{tTJ} in Ringer's solution to the "background effect" from neighboring bTJs. When small ions

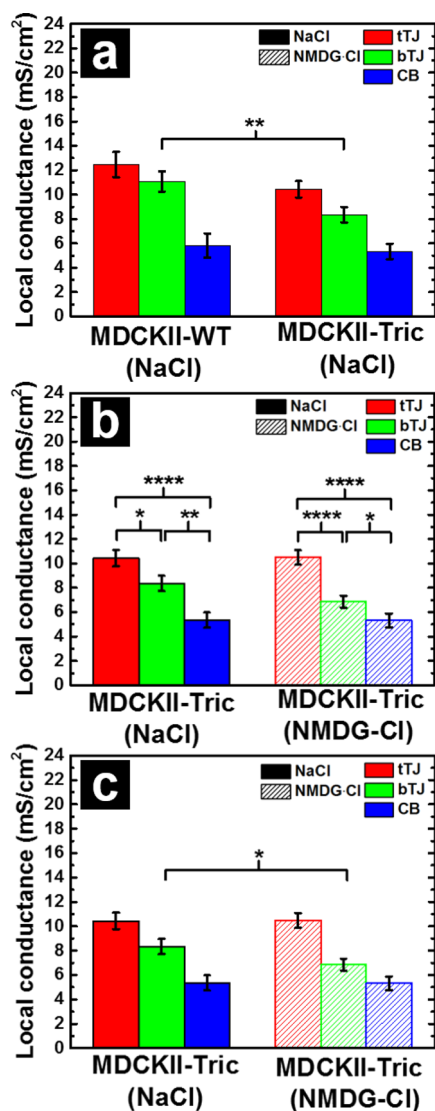


Figure 5. Apparent local conductance differences induced by tricellulin overexpression in MDCKII cells (a). Decreases in G^{tTJ} ($p = 0.1$) and G^{bTJ} ($p < 0.01$) were observed indicating tighter epithelium with excess tricellulin. (b) Tri- and bicellular TJ conductance show significant difference ($p < 0.05$) in tricellulin overexpression cells, and NMDG⁺ substitution further distinguished two paracellular pathways ($p < 0.0001$). This larger difference between G^{tTJ} and G^{bTJ} results from change in bTJ conductance due to the impermeability of NMDG⁺ (c). All statistical test results are in the [Supporting Information](#).

are substituted with larger ones (NMDG⁺ here), a trend similar to that observed for MDCKII-WT cells is observed for MDCKII-Tric cells (Figure 5b,c). NMDG⁺ substitution resulted in a significant reduction in G^{bTJ} as bTJs are impermeable to NMDG⁺ while G^{tTJ} remained the same, which further confirms overexpression of tricellulin did not alter tTJ transport properties. Together, these data demonstrate P-SICM allows the discrimination of tricellulin effects on bTJ and tTJ transport.

Further Considerations. The primary challenge in tTJ analysis is to discriminate between tTJs and flanking bTJs. With P-SICM, the rare tTJ conductance in an epithelium can be captured and distinguished from bTJ conductance; however, a pure separation of the two paracellular pathways is still not

achieved due to the “background” interference from neighboring bTJs mentioned above. There are several important experimental and physical parameters of these measurements that bear further consideration.

Localized paracellular transport can be viewed in terms of forming a “virtual megaohm seal” between the P-SICM probe and TJs, similar in some aspects to the loose-patch approach from electrophysiology.^{46,47} In SICM, this seal is normally referred to as the “access resistance” (typical magnitude of few megaohms) originates from the hindrance of ion flow between the narrow gap between the nanopipet tip and cell surface.^{48,49} Thus, the “background” signal in P-SICM can be more easily understood as current leaking through the “megaohm seal” or, in the context of electric field, a partial overlap of electric field above adjacent transport pathways. To estimate this effect, a classical model proposed by Newman for potential distribution above a disk electrode can be used.⁴⁰ In this model, a bTJ channel is treated as a circular nanopore with a diameter of 7 Å, analogous to a planar metal disk electrode. As a transepithelial potential (V_{TM}) is applied, a potential gradient is generated above the bTJ pore. In the potential profile at $D_{ps} = 200$ nm (a reasonable D_{ps} for P-SICM recording), which is constructed by plotting the normalized potential with respect to the potential over pore center versus the lateral distance from pore center, a rapid decay to 10% of the value at local electric field center is observed within 2 μm (Figure S5, [Supporting Information](#)). From previous experimental results²² and using the simplest estimation, a bTJ pore spacing of 500 nm (average length per bTJ pore along the cell perimeter, see [Supporting Information](#)) from the tTJ center can be estimated. Of note, previous estimates of bTJ spacing are as close as 25 nm; however, both of these numbers (500 and 25 nm spacing) originate from the difference between WT and claudin-2 depleted cell lines. Protein expression measurement for cell lines used here confirmed significantly depleted claudin levels for tricellulin overexpression cells, relative to WT, which likely makes the claudin spacing larger. As an estimation if we consider the case of bTJ pores spaced at 500 nm, the local field from such neighboring bTJ pores decays to <40% of the maximum bTJ field strength. Overlapping fields from multiple conductive pathways in the probe sensing zone can also result in broader measurement distributions, as compared to the normal distribution expected from junction dynamics and random errors in measurement. To sense a more confined field and exclude effects from neighboring conductive pathways, a smaller D_{ps} can be chosen by utilizing a smaller tip or by controlling the probe at a higher feedback set point.⁴⁹

An additional contributing factor to the broad distribution is from the mathematical model used for calculation of G values. Equation 1 can be written in a more general form as, where G is determined by the local electric field E divided by electrolyte resistivity and applied transepithelial excitation V_{TM} . In P-SICM, the local electric field is assessed by the average potential gradient (for experiments here, in the D_{ps} range of 200 nm to 12.5 μm) by dividing the potential difference measured at the two heights over the total displacement of probe in the z direction. A closer examination of the local potential field distribution above a nanopore with the Newman model (Figure S5b, [Supporting Information](#)) reveals an obvious nonlinearity in the local potential gradient along the z axis above a nanopore (or transport pathway). To obtain more accurate measurements of the apparent conductance of individual conductive pathways, P-SICM recordings taken at multiple D_{ps} will allow

multiple local potential recordings which can be used to determine the nonlinearity of the electric field. For experiments here, since the application of ac V_{TM} can cause fluctuations in ion current and hence affect the pipet z position during imaging and measurement, manual positioning of the pipet to the desired x , y , and z locations followed by measurements at fixed D_{ps} with turning off SICM feedback control was required. The present approach results in increase in recording time. We are working to integrate automated measurement within the feedback routine, in an effort to overcome this shortcoming. Specifically, pausing feedback control during imaging at desired D_{ps} while simultaneously triggering on V_{TM} to create an interlaced potentiometric/topographic image is under development.

CONCLUSIONS

With P-SICM, measurements of local conductance differences between tTJ and bTJ areas in a cell monolayer have been demonstrated for the first time. Heterogeneity in paracellular conductive pathways (bTJ vs tTJ) has been identified. tTJs are permeable to large organic ions, NMDG⁺, which cannot permeate bTJs. Overexpression of tricellulin, a TJ protein concentrated at tTJs, induced a significant decrease in paracellular conductance indicating the role of tricellulin in epithelial barrier function. The effect of tricellulin on G^{bTJ} was also observed to be more significant than for G^{tTJ} due to the perturbation of claudin expression. P-SICM provides a tool to discriminate such differences in conductance not easily achieved by other routes. The ability of P-SICM to detect rare conductance in live cells is afforded by the high spatial resolution of SICM and sensitivity of potentiometric measurements. While the present manuscript is aimed at understanding instrumental limitations to measurement of cell monolayer conductances, samples used here showed overexpression of tricellulin significantly reduced the gene expression of claudin-2 (Figures S3 and S4), which is assumed to be responsible for the reduction in bTJ conductance. Previous studies have found tricellulin and claudin expression to be related, and this presents intriguing biochemical questions which P-SICM may be used to address in the future.^{12,50,51} Thus, the intricate interdependence of bTJ and tTJ molecular components (e.g., tricellulin and claudins) further emphasizes the future utility of P-SICM for delineation of the role of each of junctional proteins in bTJ versus tTJ conductance.

ASSOCIATED CONTENT

Supporting Information

The Supporting Information is available free of charge on the ACS Publications website at DOI: 10.1021/acs.analchem.6b02392.

Additional experimental details, FACS cell sorting, Western blot analyses, immunolabeling fluorescence images, local potential filed simulations, and statistical analysis (PDF)

AUTHOR INFORMATION

Corresponding Authors

*Phone: (812) 856-1873. Fax: (812) 856-8300. E-mail: lanbaker@indiana.edu.

*Phone: (314) 362-5685. Fax: (314) 362-8237. E-mail: jhou@dom.wustl.edu.

Notes

The authors declare no competing financial interest.

ACKNOWLEDGMENTS

We thank Washington University light microscopy and electron microscopy core for assistance. This work was supported by grants from NIDDK, Grant R01DK084059, the American Heart Association, Grant 0930050N, and the Department of Defense, Grant HDTRA1-11-16-BRCWMBAA.

REFERENCES

- (1) Farquhar, M. G.; Palade, G. E. *J. Cell Biol.* **1963**, *17*, 375–412.
- (2) Stevenson, B. R.; Siliciano, J. D.; Mooseker, M. S.; Goodenough, D. A. *J. Cell Biol.* **1986**, *103*, 755–766.
- (3) Tsukita, S.; Furuse, M.; Itoh, M. *Nat. Rev. Mol. Cell Biol.* **2001**, *2*, 285–293.
- (4) Furuse, M.; Fujita, K.; Hiiragi, T.; Fujimoto, K.; Tsukita, S. *J. Cell Biol.* **1998**, *141*, 1539–1550.
- (5) Furuse, M.; Tsukita, S. *Trends Cell Biol.* **2006**, *16*, 181–188.
- (6) Ikenouchi, J.; Furuse, M.; Furuse, K.; Sasaki, H.; Tsukita, S.; Tsukita, S. *J. Cell Biol.* **2005**, *171*, 939–945.
- (7) Watson, C. J.; Rowland, M.; Warhurst, G. *Am. J. Physiol.: Cell Physiol.* **2001**, *281*, C388–C397.
- (8) Tang, V. W.; Goodenough, D. A. *Biophys. J.* **2003**, *84*, 1660–1673.
- (9) Yu, A. S.; Cheng, M. H.; Angelow, S.; Gunzel, D.; Kanzawa, S. A.; Schneeberger, E. E.; Fromm, M.; Coalson, R. D. *J. Gen. Physiol.* **2009**, *133*, 111–127.
- (10) Staehelin, L. A. *J. Cell Sci.* **1973**, *13*, 763–786.
- (11) Walker, D. C.; MacKenzie, A.; Hulbert, W. C.; Hogg, J. C. *Cells Tissues Organs* **1985**, *122*, 35–38.
- (12) Krug, S. M.; Amasheh, S.; Richter, J. F.; Milatz, S.; Gunzel, D.; Westphal, J. K.; Huber, O.; Schulzke, J. D.; Fromm, M. *Mol. Biol. Cell* **2009**, *20*, 3713–3724.
- (13) Cereijido, M.; Gonzalez-Mariscal, L.; Borboa, L. *J. Exp. Biol.* **1983**, *106*, 205–215.
- (14) Van Itallie, C. M.; Holmes, J.; Bridges, A.; Gookin, J. L.; Coccato, M. R.; Proctor, W.; Colegio, O. R.; Anderson, J. M. *J. Cell Sci.* **2008**, *121*, 298–305.
- (15) Benson, K.; Cramer, S.; Galla, H.-J. *Fluids Barriers CNS* **2013**, *10*, 5.
- (16) Van Driessche, W.; Kreindler, J. L.; Malik, A. B.; Margulies, S.; Lewis, S. A.; Kim, K.-J. *Am. J. Physiol.: Lung Cell. Mol. Physiol.* **2007**, *293*, L520–L524.
- (17) Günzel, D.; Zakrzewski, S. S.; Schmid, T.; Pangalos, M.; Wiedenhoef, J.; Blasse, C.; Ozboda, C.; Krug, S. M. *Ann. N. Y. Acad. Sci.* **2012**, *1257*, 142–151.
- (18) Krug, S. M.; Fromm, M.; Günzel, D. *Biophys. J.* **2009**, *97*, 2202–2211.
- (19) Gitter, H. A.; Bertog, M.; Schulzke, J.-D.; Fromm, M. *Pfluegers Arch.* **1997**, *434*, 830–840.
- (20) Florian, P.; Schöneberg, T.; Schulzke, J. D.; Fromm, M.; Gitter, A. H. *J. Physiol.* **2002**, *545*, 485–499.
- (21) Gitter, A. H.; Wullstein, F.; Fromm, M.; Schulzke, J. D. *Gastroenterology* **2001**, *121*, 1320–1328.
- (22) Chen, C.-C.; Zhou, Y.; Morris, C. A.; Hou, J.; Baker, L. A. *Anal. Chem.* **2013**, *85*, 3621–3628.
- (23) Hansma, P.; Drake, B.; Marti, O.; Gould, S.; Prater, C. *Science* **1989**, *243*, 641–643.
- (24) Zhou, Y.; Chen, C.-C.; Weber, A. E.; Zhou, L.; Baker, L. A. *Langmuir* **2014**, *30*, 5669–5675.
- (25) Gong, Y.; Renigunta, V.; Zhou, Y.; Sunq, A.; Wang, J.; Yang, J.; Renigunta, A.; Baker, L. A.; Hou, J. *Mol. Biol. Cell* **2015**, *26*, 4333–4346.
- (26) Schlüter, H.; Moll, I.; Wolburg, H.; Franke, W. W. *Eur. J. Cell Biol.* **2007**, *86*, 645–655.
- (27) Riazuddin, S.; Ahmed, Z. M.; Fanning, A. S.; Lagziel, A.; Kitajiri, S.-i.; Ramzan, K.; Khan, S. N.; Chattaraj, P.; Friedman, P. L.;

- Anderson, J. M.; Belyantseva, I. A.; Forge, A.; Riazuddin, S.; Friedman, T. B. *Am. J. Hum. Genet.* **2006**, *79*, 1040–1051.
- (28) Raleigh, D. R.; Marchiando, A. M.; Zhang, Y.; Shen, L.; Sasaki, H.; Wang, Y.; Long, M.; Turner, J. R. *Mol. Biol. Cell* **2010**, *21*, 1200–1213.
- (29) Nayak, G.; Lee, S. I.; Yousaf, R.; Edelmann, S. E.; Trincot, C.; Van Itallie, C. M.; Sinha, G. P.; Rafeeq, M.; Jones, S. M.; Belyantseva, I. A.; Anderson, J. M.; Forge, A.; Frolenkov, G. I.; Riazuddin, S. *J. Clin. Invest.* **2013**, *123*, 4036–4049.
- (30) Cereijido, M.; Stefani, E.; Palomo, A. *J. Membr. Biol.* **1980**, *53*, 19–32.
- (31) Yu, A. S. L.; Enck, A. H.; Lencer, W. I.; Schneeberger, E. E. *J. Biol. Chem.* **2003**, *278*, 17350–17359.
- (32) Broughman, J. R.; Brandt, R. M.; Hastings, C.; Iwamoto, T.; Tomich, J. M.; Schultz, B. D. *Am. J. Physiol.: Cell Physiol.* **2004**, *286*, C1312–C1323.
- (33) Nagpal, R.; Patel, A.; Gibson, M. C. *BioEssays* **2008**, *30*, 260–266.
- (34) Aegerter-Wilmsen, T.; Smith, A. C.; Christen, A. J.; Aegerter, C. M.; Hafen, E.; Basler, K. *Development* **2010**, *137*, 499–506.
- (35) Rheinlaender, J.; Schäffer, T. E. *Anal. Chem.* **2015**, *87*, 7117–7124.
- (36) Weber, A. E.; Baker, L. A. *J. Electrochem. Soc.* **2014**, *161*, H924–H929.
- (37) Rheinlaender, J.; Schäffer, T. E. *J. Appl. Phys.* **2009**, *105*, 094905.
- (38) Edwards, M. A.; Williams, C. G.; Whitworth, A. L.; Unwin, P. R. *Anal. Chem.* **2009**, *81*, 4482–4492.
- (39) Del Linz, S.; Willman, E.; Caldwell, M.; Klenerman, D.; Fernández, A.; Moss, G. *Anal. Chem.* **2014**, *86*, 2353–2360.
- (40) Newman, J. J. *J. Electrochem. Soc.* **1966**, *113*, 501–502.
- (41) Zhou, L.; Zeng, Y.; Baker, L. A.; Hou, J. *Tissue Barriers* **2015**, *3*, e1105907.
- (42) Van Itallie, C. M.; Rahner, C.; Anderson, J. M. *J. Clin. Invest.* **2001**, *107*, 1319–1327.
- (43) Colegio, O. R.; Van Itallie, C. M.; McCrea, H. J.; Rahner, C.; Anderson, J. M. *Am. J. Physiol.: Cell Physiol.* **2002**, *283*, C142–C147.
- (44) Ben-Yosef, T.; Belyantseva, I. A.; Saunders, T. L.; Hughes, E. D.; Kawamoto, K.; Van Itallie, C. M.; Beyer, L. A.; Halsey, K.; Gardner, D. J.; Wilcox, E. R.; Rasmussen, J.; Anderson, J. M.; Dolan, D. F.; Forge, A.; Raphael, Y.; Camper, S. A.; Friedman, T. B. *Hum. Mol. Genet.* **2003**, *12*, 2049–2061.
- (45) Wen, H.; Watry, D. D.; Marcondes, M. C. G.; Fox, H. S. *Mol. Cell. Biol.* **2004**, *24*, 8408–8417.
- (46) Almers, W.; Stanfield, P. R.; Stühmer, W. *J. Physiol.* **1983**, *336*, 261–284.
- (47) Strickholm, A. *J. Gen. Physiol.* **1961**, *44*, 1073–1088.
- (48) Nitz, H.; Kamp, J.; Fuchs, H. *Probe Microsc.* **1998**, *1*, 187–200.
- (49) Chen, C.-C.; Zhou, Y.; Baker, L. A. *Annu. Rev. Anal. Chem.* **2012**, *5*, 207–228.
- (50) Cording, J.; Berg, J.; Käding, N.; Bellmann, C.; Tscheik, C.; Westphal, J. K.; Milatz, S.; Günzel, D.; Wolburg, H.; Piontek, J.; Huber, O.; Blasig, I. E. *J. Cell Sci.* **2013**, *126*, 554–564.
- (51) Mandon, M.; Cyr, D. G. *Biol. Reprod.* **2015**, *92* (3), 66.